Supplementary Materials for "**Photonic axion insulator with non-coplanar chiral hinge transport**"

Hua-Shan Lai[1], Yan-Chen Zhou[1], Ze-Qun Sun[1], Cheng He[1,2,3*], Yan-Feng Chen,[1,2,3†]

[1]National Laboratory of Solid State Microstructures & Department of Materials Science and Engineering, Nanjing University, Nanjing 210093, China

[2]Collaborative Innovation Center of Advanced Microstructures, Nanjing University, Nanjing 210093, China

[3]Jiangsu Key Laboratory of Artificial Functional Materials, Nanjing University, Nanjing 210093, China.

Content for supplementary figures:

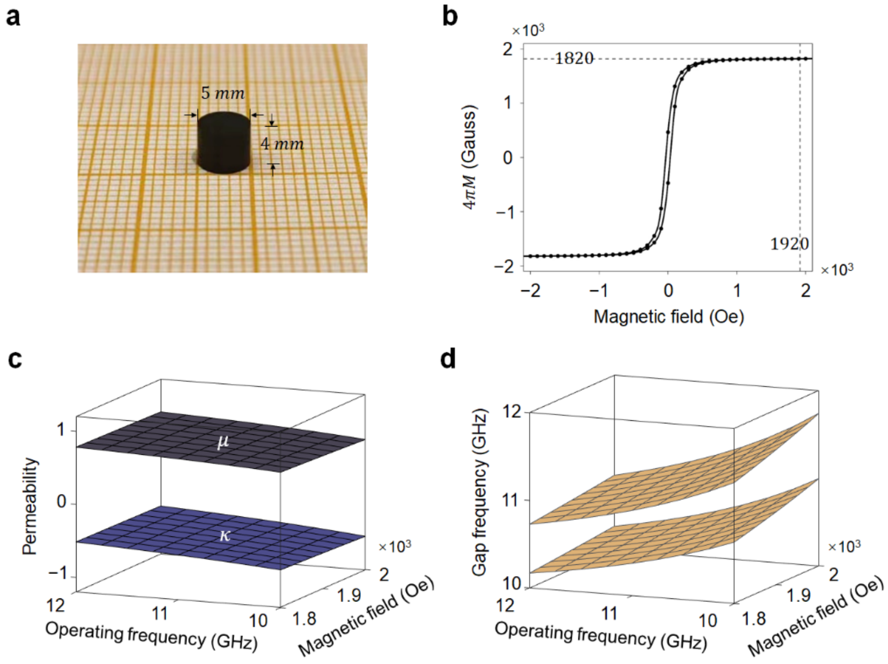

Supplementary Fig. 1 | Parameters of YIG ferrites. a, Photograph of a YIG rod. **b,** Measured magnetic curve of YIG ferrites. **c,** Magnetic field and operating frequency dependent permeability components μ and κ of YIG materials. **d,** The corresponding bulk bandgap at the Brillouin centre (frequency window between two surfaces).

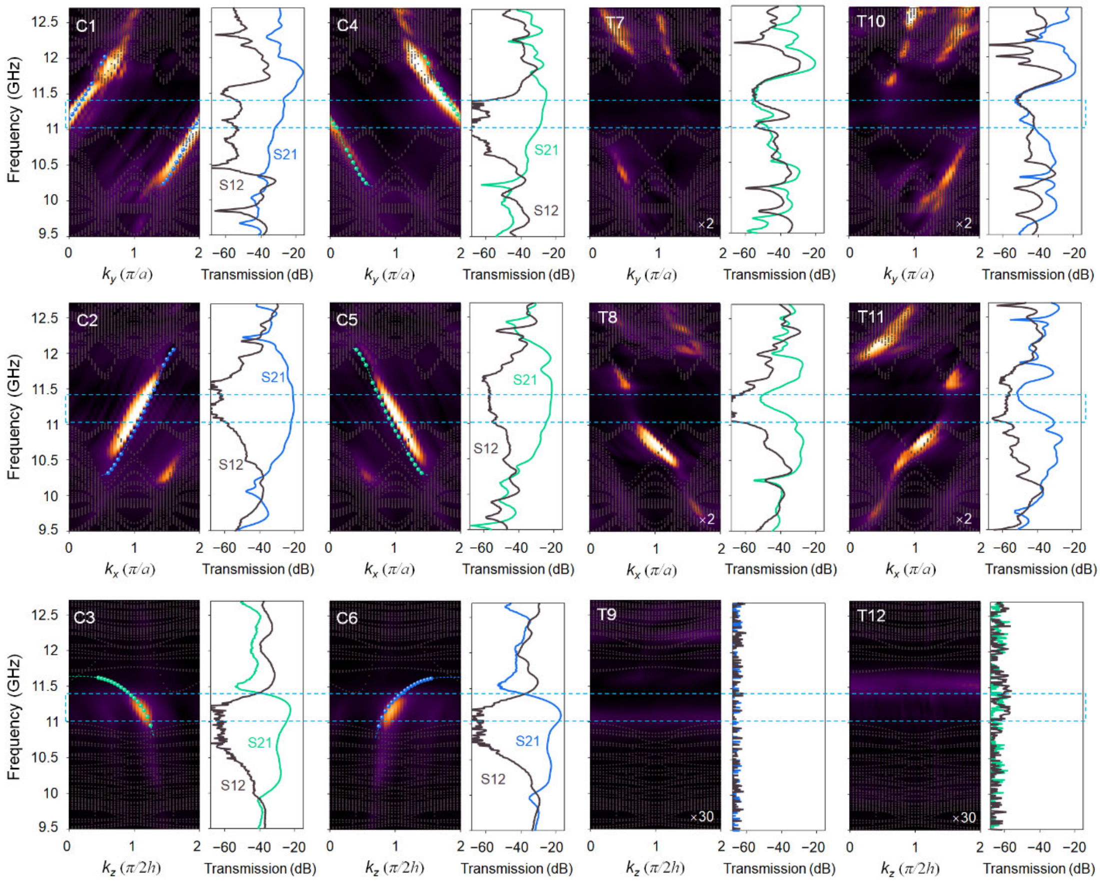

Supplementary Fig. 2 | Measured non-reciprocal hinge transmission spectra. Measured forward and backward hinge transmission spectra (right subpanels) for C1-C6 and T7-T12, corresponding to hinge dispersions (left subpanels) in Fig. 3c based on S_{21} parameters. For comparison, blue dashed boxes indicate the complete bandgap. The hinge transmissions are recorded after propagating 12a, 12a, and 8h distances along the y, x, and z directions, respectively.

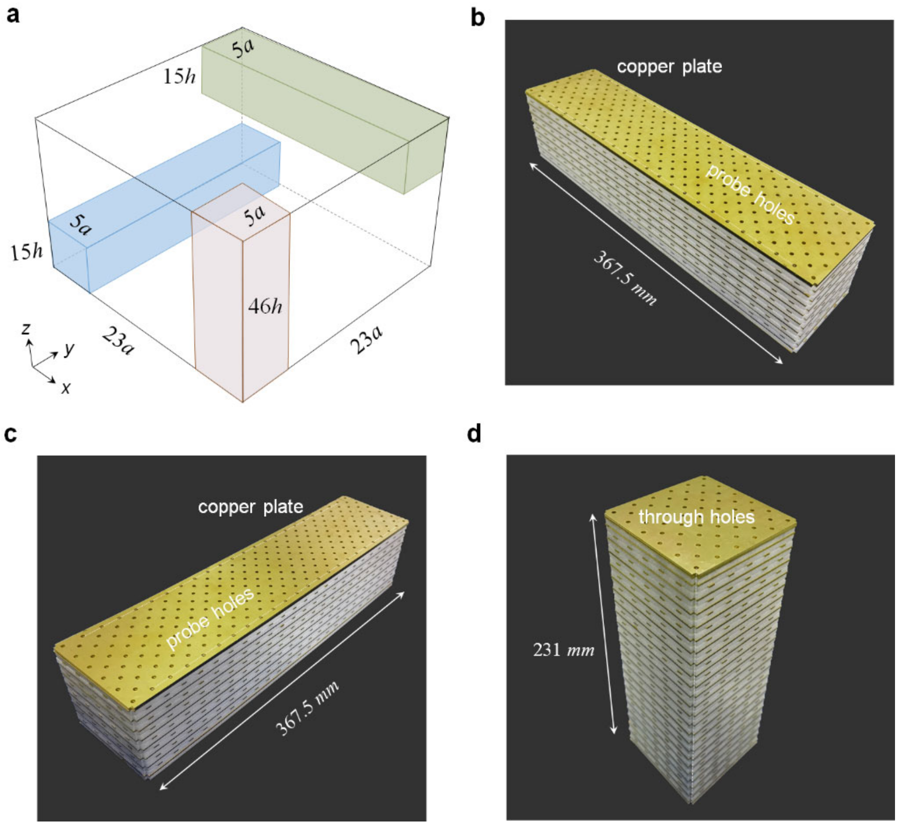

Supplementary Fig. 3 | Photographs of experimental samples. a, Schematic of a $23a\times23a\times46h$ sample divided into three parts. **b,** Picture of $23a\times5a\times15h$ experimental sample to measure k_x-hinge dispersion. **c,** Picture of $5a\times23a\times15h$ experimental sample to measure k_y-hinge dispersion. **d**, Picture of $5a\times5a\times46h$ experimental sample to measure k_z-hinge dispersion.

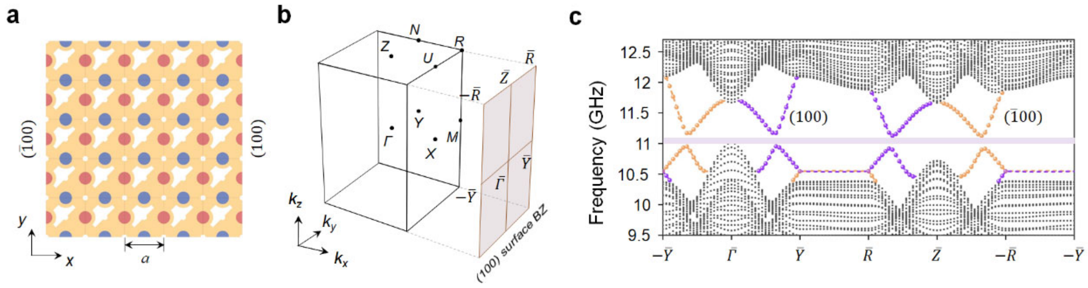

Supplementary Fig. 4 | Surface states for intact boundary condition. a, Top-view of the AB interlayer. Using unit cells in Fig.2a to construct a whole sample, the surface rods are semi-cylinders. **b,** Projected Brillouin zone on the lateral surface. **c,** Projected band structures. Black dots denote the bulk states. Purple and yellow dots denote the lateral surface states. The highlight region denotes the complete bandgap for chiral hinge states.

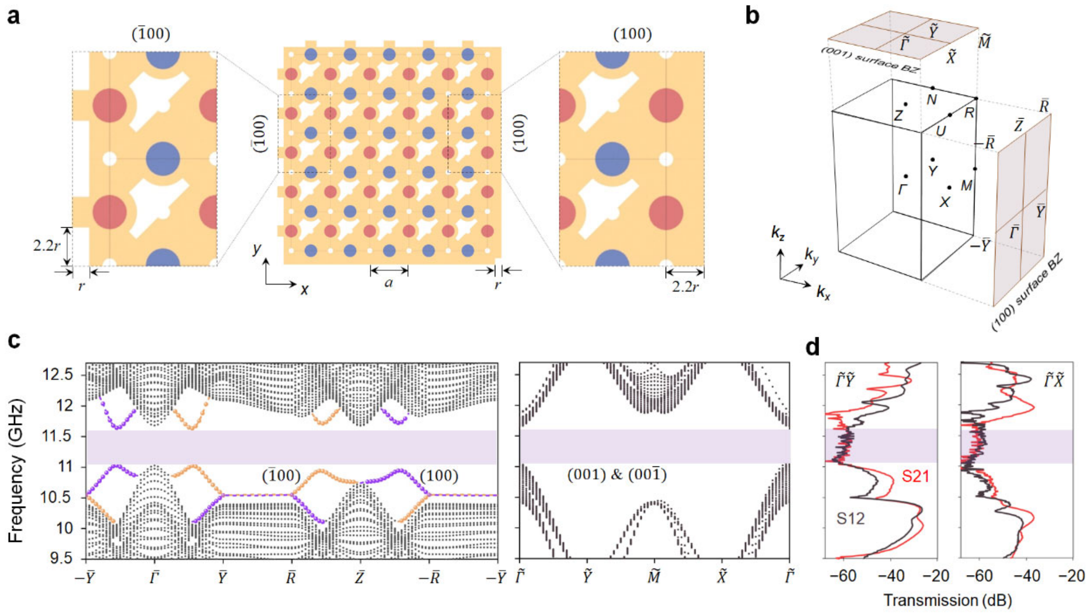

Supplementary Fig. 5 | Surface modification to enlarge the complete bandgap. a, modified surfaces of the AB interlayers. BA interlayers are accordingly modified under inversion symmetry. Squared-through holes (including dielectric foams) are drilled at corners to enhance the *z*-directional hinge transport. **b,** Projected Brillouin zone. **c,** Projected band structures. Purple and yellow dots denote surface states. **d,** Measured surface transmission spectra. The highlight regions denote the complete bandgap.

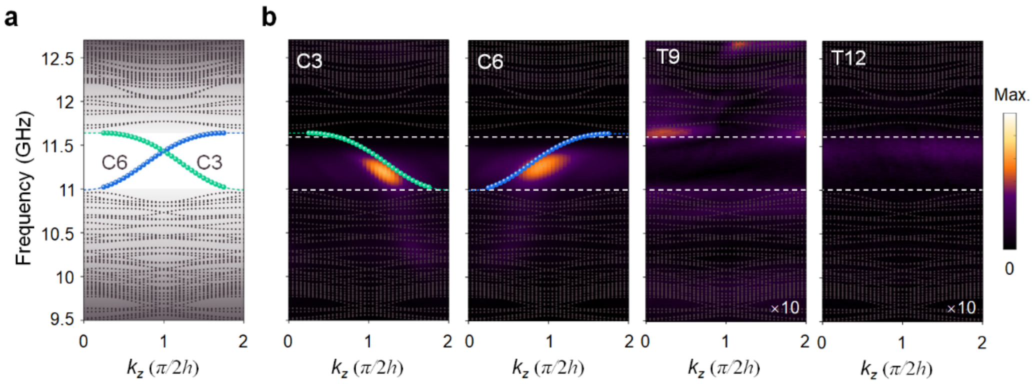

Supplementary Fig. 6 | Hinge decoration to suppress trivial hinge states. a, Calculated k_z-hinge states after removing squared-through holes at the corners along the z axis. The trivial hinges in the right panel of Fig. 3b are suppressed. **b,** Measured hinge dispersions of four z-axis hinges C3, C6, T9, and T12. The flat-band effect brings weaker upper branches measured for hinges C3 and C6 in experiments.

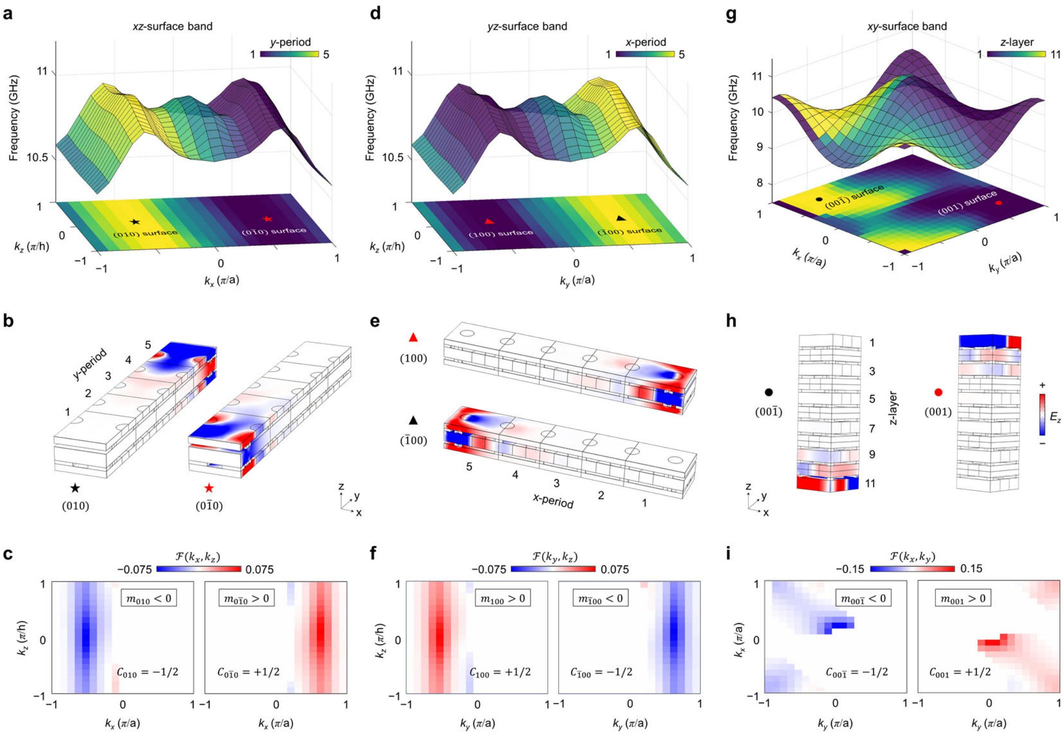

Supplementary Fig. 7 | Surface Dirac masses of our photonic AXI. a, The *xz*-surface band below the bandgap, including both the (010) and ($0\bar{1}0$) surface states. Colorscale presents the contribution of all states to the (010) surface (denoted as period 5) and ($0\bar{1}0$) surface (period 1). **b,** Field distribution of the (010) and ($0\bar{1}0$) surface modes. **c,** Numerically calculated Berry curvature $\mathcal{F}(k_x, k_z)$. The opposite signs of Berry curvature near the valley indicate the opposite Dirac masses for opposite surfaces. The integration of Berry curvature gives the surface Chern number $C_{\boldsymbol{n}} = \pm 1/2$, equivalent to $sign(m_{\boldsymbol{n}})/2$, where the subscript ***n*** represents surface normal. **d-f,** The *yz*-surface case. **g-i,** The *xy*-surface case. Therefore, on the hinge between two neighbouring surfaces with opposite Dirac masses, the differences of surface Chern number results in a topological invariant $\Delta C_{\boldsymbol{n}} = \pm 1$, leading to the existence of topological hinge states (the sign of $\Delta C_{\boldsymbol{n}}$ determines the direction of energy flow).

For the photonic axion insulator, due to the broken time-reversal symmetry, all the surface states are gapped and will acquire finite masses (m), whose signs depend on the signs of the Berry curvature of the lower-energy surface states.

Here, we numerically calculate the Berry curvature for each surface state, as shown in Supplementary Fig. 7. Taking the *xz* surface as an example, the surface band below the bandgap (Supplementary Fig.7a) includes both (010) and ($0\bar{1}0$) surface states, which are symmetrically distributed in half of the Brillouin zone enforced by inversion symmetry (Supplementary Fig.7b). However, their Berry curvatures exhibit opposite values around different valleys due to the simultaneous breaking of time-reversal symmetry and mirror symmetry, resulting in opposite signs of Dirac masses for opposite surfaces (Supplementary Fig.7c). Similarly, we also calculate the *yz*-surface and *xy*-surface cases [Supplementary Fig.7(d-f) and Supplementary Fig.7(g-i)], consistent with the mass distributions in Fig. 1c in the main text.

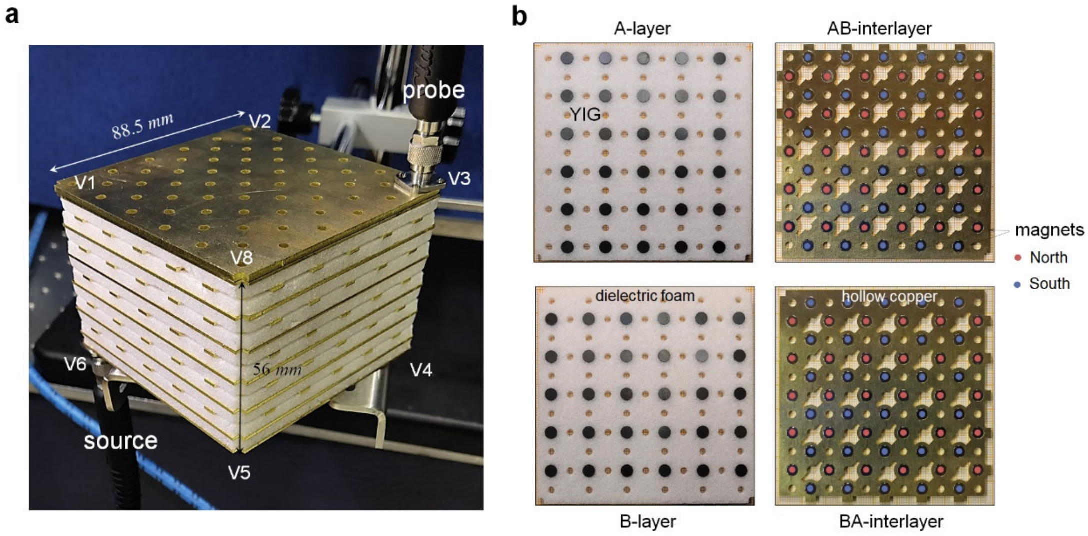

Supplementary Fig. 8 | Experimental set-up for chiral hinge transport. a, Experiment set-up for measuring hinge transport in Fig. 4. The sample has $5a\times5a\times11h$ size. **b,** Top-view pictures of A-layer, B-layer, AB-interlayer, and BA-interlayer. Red (blue) dots mark the north (south) polarity of magnets.

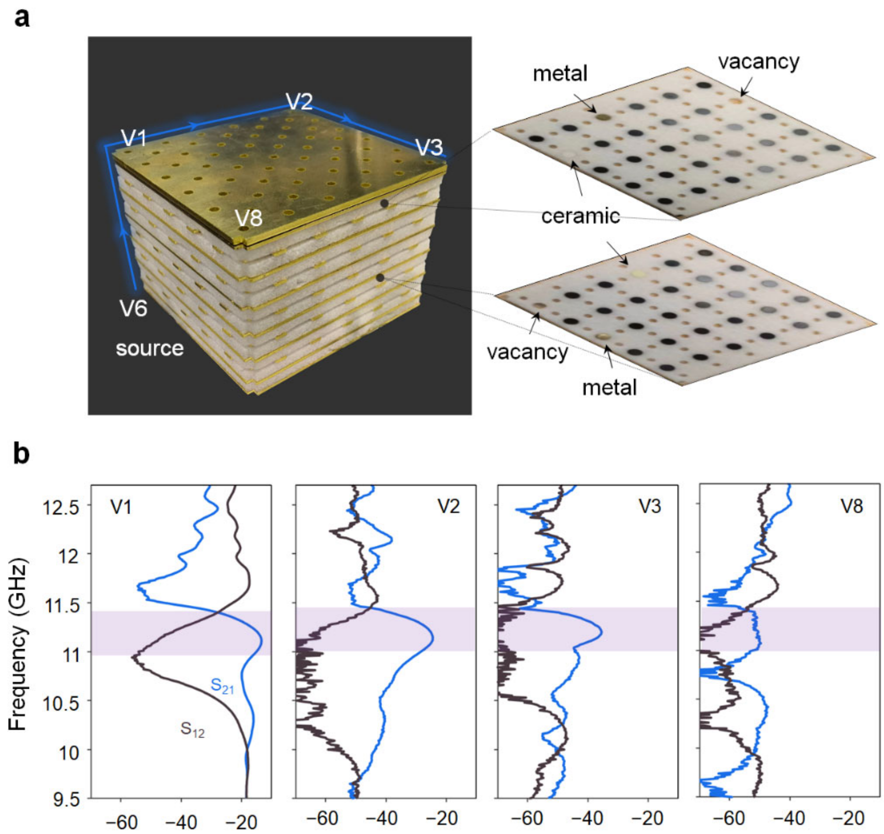

Supplementary Fig. 9 | Robustness of chiral hinge transport. a, Experiment set-up for checking the robustness of chiral hinge transport against various defects, such as vacancy, ceramic rods (Al_2O_3 with relative permittivity of 10), and metal rods (copper). **b,** Measured transmission spectra at V1-V3, and V8 vertices, excited via V6 vertex. Although slightly enhanced intensity at the trivial V8 vertex is due to the increased finite size effect under scattering (compared to Fig. 4b), it is still 20 dB weaker than that of the V2 vertex with the same propagating distance.

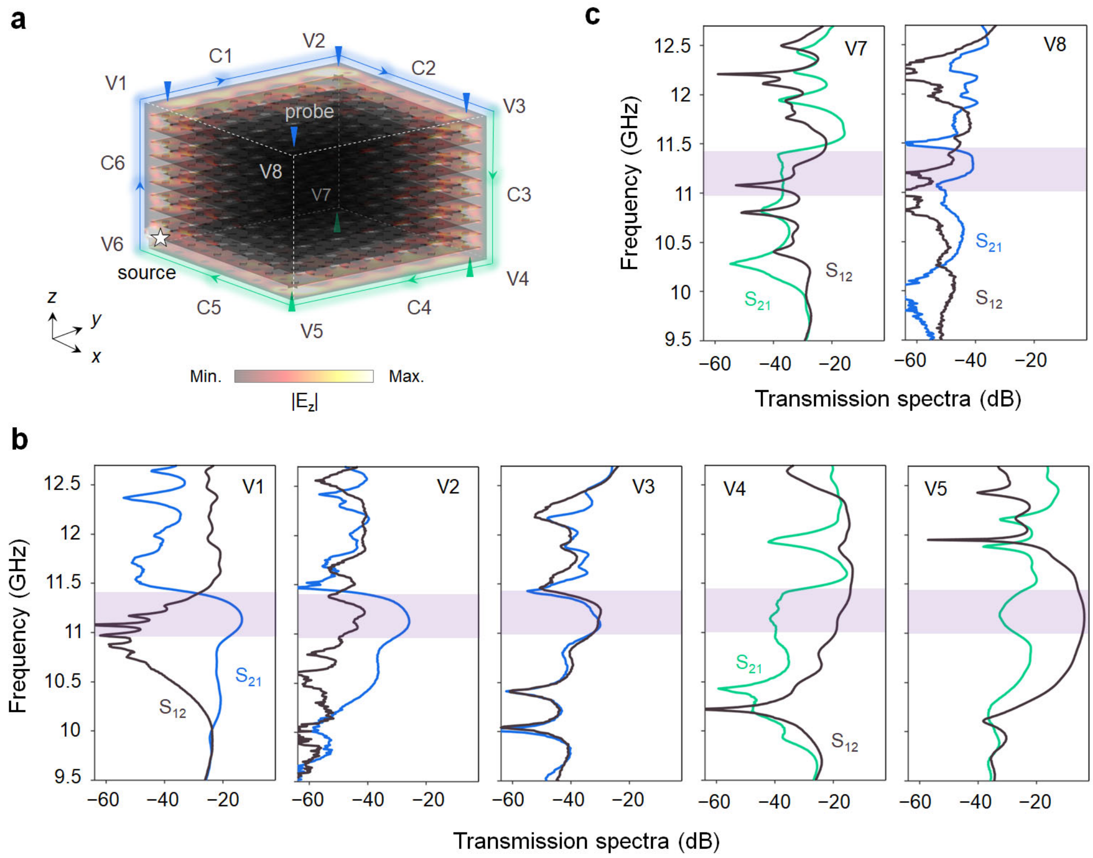

Supplementary Fig. 10 | Closed loop scenario for chiral hinge transport. a, Simulated field distribution of closed chiral hinge loop at the frequency of 11.2 GHz, excited via the V6 vertex. All facets are perfect conductor boundary conditions. **b,** Measured transmission spectra at V1-V5 vertices, all located on the way of the chiral loop. The nearly equal S_{21} and S_{12} parameters at the V3 vertex are non-reciprocal due to different chiral routes, i.e., one is along V6-C6-C1-C2-V3 (blue arrows), and the other is along V3-C3-C4-C5-V6 (green arrows). **c,** Measured transmission spectra at V7 and V8 vertices outside of the chiral loop.

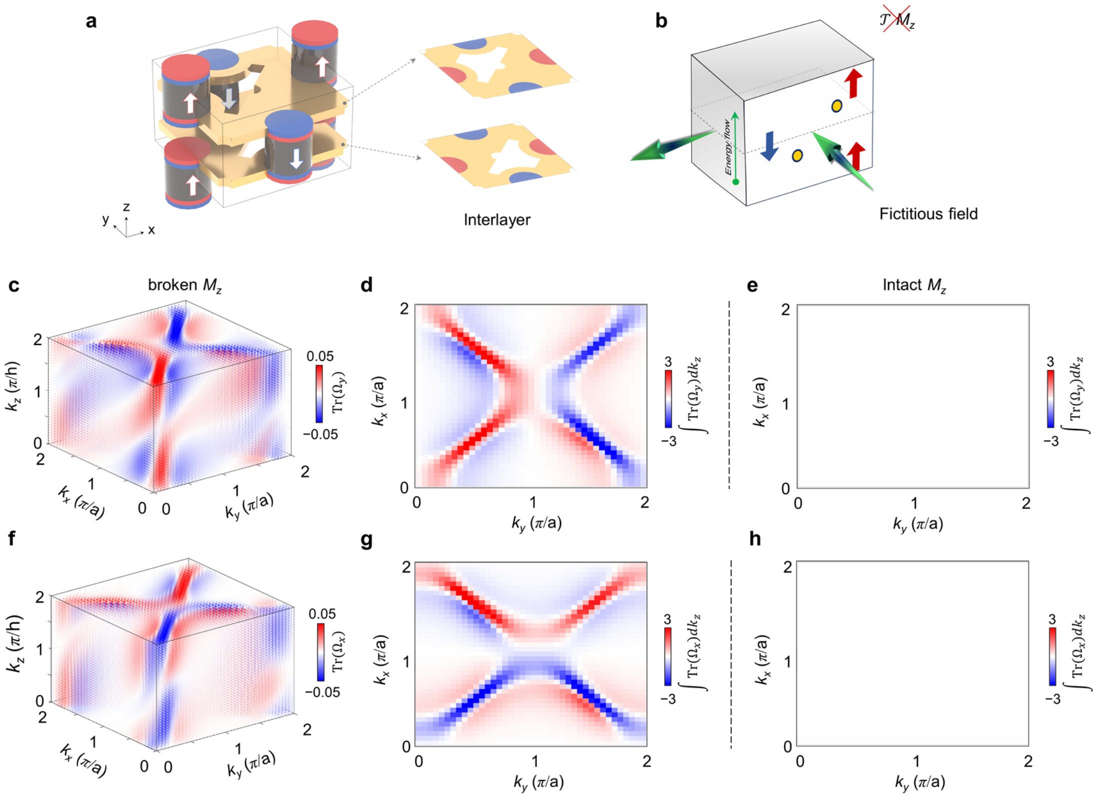

Supplementary Fig. 11 | Fictitious fields induced by nontrivial Berry curvature. a, Unit cell of our photonic axion insulator. The magnetizations break the time-reversal symmetry ($\mathcal{T}$) and the directional interlayer structures break the mirror symmetry along the *z* axis (M_z). **b,** Schematic of in-plane fictitious fields depending on nontrivial Berry curvature with broken $\mathcal{T}M_z$ symmetry. **c-d,** The *y*-component Berry curvature (Ω_y) and its integral along the k_z axis for the tight-binding model $H(k)$ (as outlined in Methods Section in the main text). The nontrivial values suggest the existence of a fictitious field in the *y* direction. The sign of the field relies on the sign of the integral of Berry curvature over the entire Brillouin zone. **e,** Trivial case with unbroken M_z symmetry [*i.e.*, the interlayer couplings t_4 and t_5 (Supplementary Fig. 13a) equal to zero], where no fictitious field can be found corresponding to vanishing Ω_y values. **f-h,** The same as **c-e** except with the *x*-component Berry curvature (Ω_x).

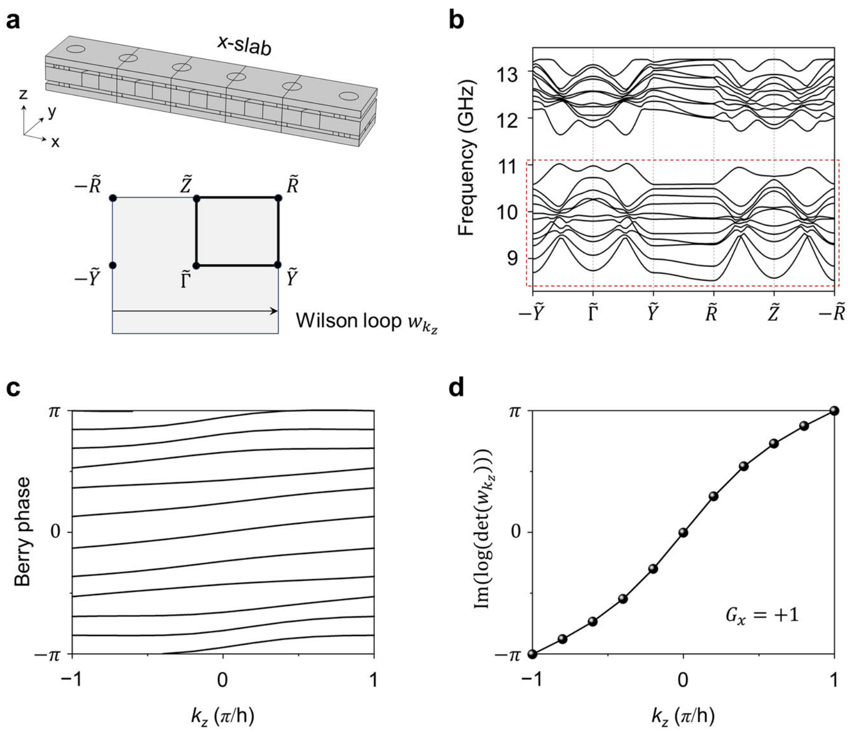

Supplementary Fig. 12 | Wilson loop spectrum for an *x*-directed slab. a, An *x*-directed slab with 5 unit cells along the *x* axis, while being periodic along the other two directions. **b**, Band structures. **c**, The k_y-directed Wilson loop spectrum for the 11 bands below the bandgap. **d**, Summation of the Wilson loop eigenvalues in **c**, exhibiting +1 winding along the k_z axis, corresponding to the nontrivial slab Chern number (G_x=1). The result implies that our system is topologically equivalent to a Chern insulator, which can possess gapless chiral states in the *z* direction when sliced into an *x*-slab geometry. Notably, the nontrivial slab Chern number can be connected to the axion angle θ: $G_x = n\nu_x + \theta/\pi$ [Ref. 45 in the main text: *Phys. Rev. B* ***98****, 245117 (2018)*]. Here, $\nu_x = 0$ denotes the weak indices of three-dimensional topological insulators, and *n* counts the units of the slab, thereby also confirming the nontrivial axion angle of $\theta = \pi$ of our photonic system.

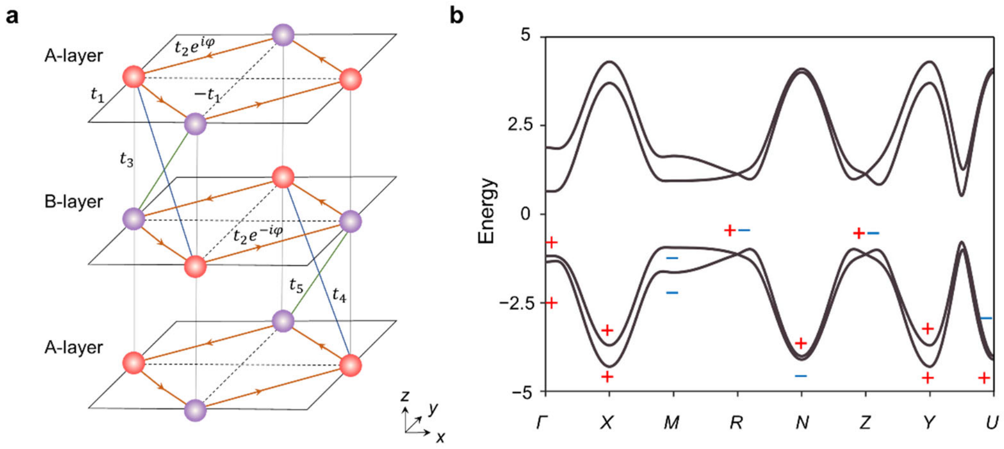

Supplementary Fig. 13 | Band structures based on tight-binding model. a, Tight-binding model for photonic AXI based on modified Haldane-like model (4-band). **b,** Bulk band structures marked with parity of eight high-symmetric points for lower two bands. These theoretical results qualitatively match with those in Fig. 2. The tight-binding parameters are: $t_1 = 1$, $t_2 = 0.4$, $t_3 = 0.15$, $t_4 = -0.1$, $t_5 = 0.45$, and $\varphi = \pi/4$.

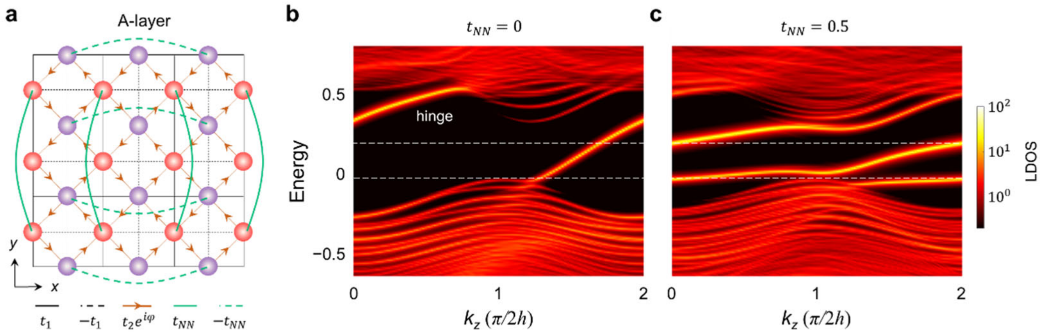

Supplementary Fig. 14 | Influence of long-range interactions. a, Tight-binding model of the A layer. The B layer is inversion symmetric to the A layer. **b-c,** The local density of state (LDOS) for the z-axis hinge state without (t_{NN}=0) and with (t_{NN}=0.5) long-range interaction. The gapless hinge states wind twice along the entire Brillouin zone when t_{NN}=0.5. The tight-binding parameters are chosen to be $t_1 = 1, t_2 = 0.4, \varphi = \pi/4$.

The long-range interactions among non-neighboring unit cells may be inevitable in electromagnetic systems. Compared to long-range interactions-induced higher-order corner states [Ref. 30 in the main text: *Nat. Photon.* **14**, 89-94 (2020)], the long-range interactions in our photonic axion insulator could not lead to new nontrivial physics but may give rise to the novel windings of gapless hinge states. Here, we consider the long-range onsite interaction (t_{NN}) in the *x*-*y* plane using the tight-binding model. Even under a relatively large long-range interaction (e.g., t_{NN}=0.5), the chiral hinge states maintain gapless (taking the z-axis hinge state as an example). In fact, in our realistic model, the long-range interaction is very weak, resulting in no winding feature of the hinge state (Fig. 3b in the main text).

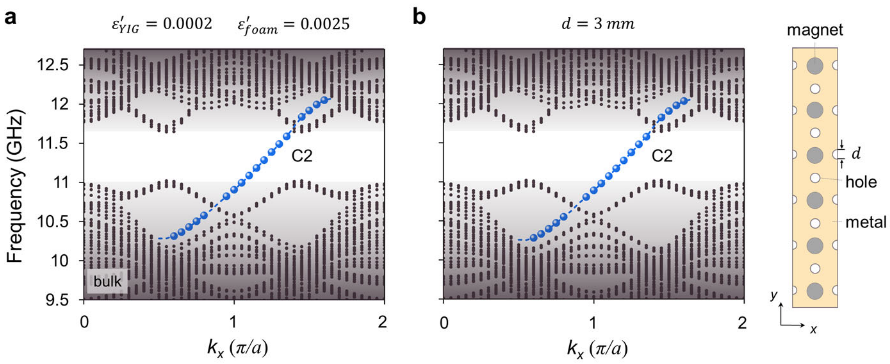

Supplementary Fig. 15 | Influence of realistic losses on C2 hinge state. a, Non-radiative loss case with $\varepsilon'_{YIG} = 0.0002$ and $\varepsilon'_{foam} = 0.0025$. The relative permittivity of YIG and foam are: $\varepsilon_{YIG} = 15 \times (1 - i\varepsilon'_{YIG})$ and $\varepsilon_{foam} = 1.05 \times (1 - i\varepsilon'_{foam})$, where imaginary terms represent the loss. **b,** Radiative loss case with *d*=3 mm. The radiative loss is introduced through the design of the circular open holes (white areas) on the top metallic plane, as shown in the right panel. Both non-radiative and radiative losses are very small, and their influence on the hinge states is negligible in our model.

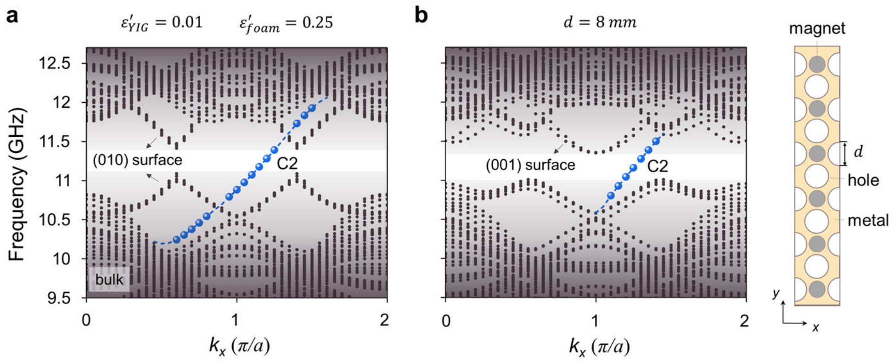

Supplementary Fig. 16 | Influence of relatively large losses on C2 hinge state. a, The non-radiative loss case with $\varepsilon'_{YIG} = 0.01$ and $\varepsilon'_{foam} = 0.25$. **b,** The radiative loss case with *d*=8 mm. In both cases, the gapless C2 hinge state exists, indicating the robustness of axion insulator phase.

Although we increase the loss to be a relatively high level, e.g., $\varepsilon'_{YIG} = 0.01$ and $\varepsilon'_{foam} = 0.25$, or *d*=8 mm, the gapless C2 hinge state still exists within the bandgap, indicating the robustness of our axion insulator phase. The increased non-radiative loss narrows the bandgap of both bulk and surface states, while the increased radiative loss only narrows the bandgap of surface states.

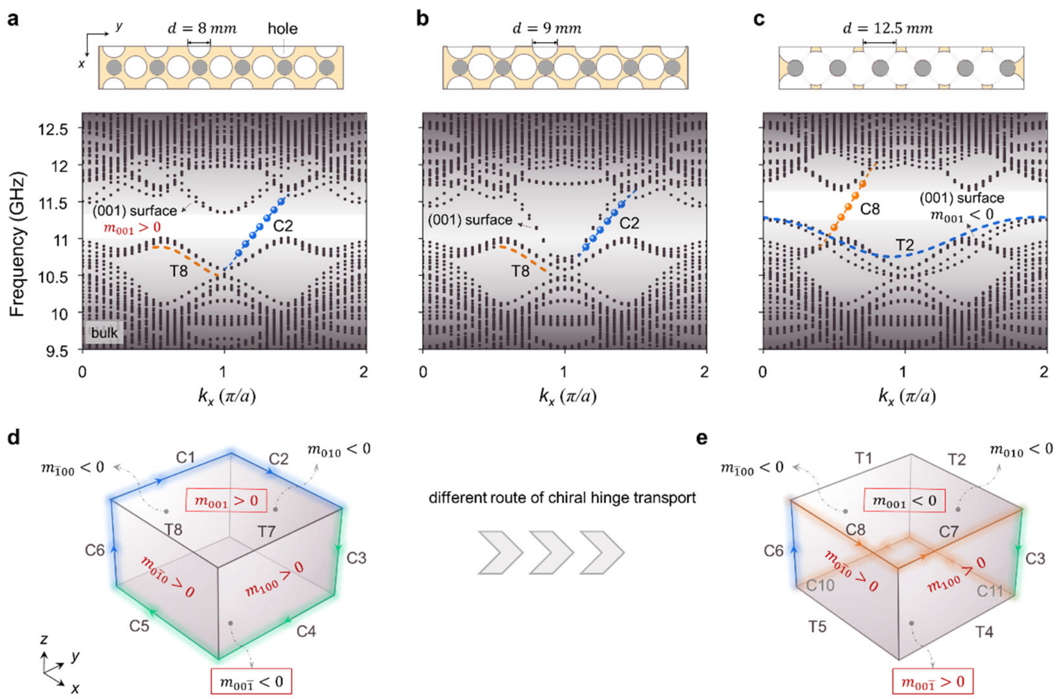

Supplementary Fig. 17 | Radiative loss-induced tunable chiral hinge transport. a-c, Hinge states under continuously increasing the radiative loss with *d*=8 mm, *d*=9 mm, and *d*=12.5 mm, respectively. **d-e,** Chiral hinge transport for case **a** and case **c**. Here, both top and bottom surfaces are applied radiative loss, *m* represents the surface Dirac mass.

The radiative loss can be considered as the surface decoration, which does not alter the bulk band structures. Therefore, the bulk topological invariant remains unchanged, but the huge radiative loss can lead to the surface band inversion (flipping the sign of surface Dirac mass). For example, if we increase the loss to *d*=12.5 mm, the originally nontrivial C2 hinge state becomes trivial T2, while the trivial T8 hinge state now becomes nontrivial C8. Similarly, we also have C1→T1, T7→C7, and vice versa (for the hinges on the bottom surface). It should be noticed that the non-coplanar chiral hinge transport still exists, but in a different route.

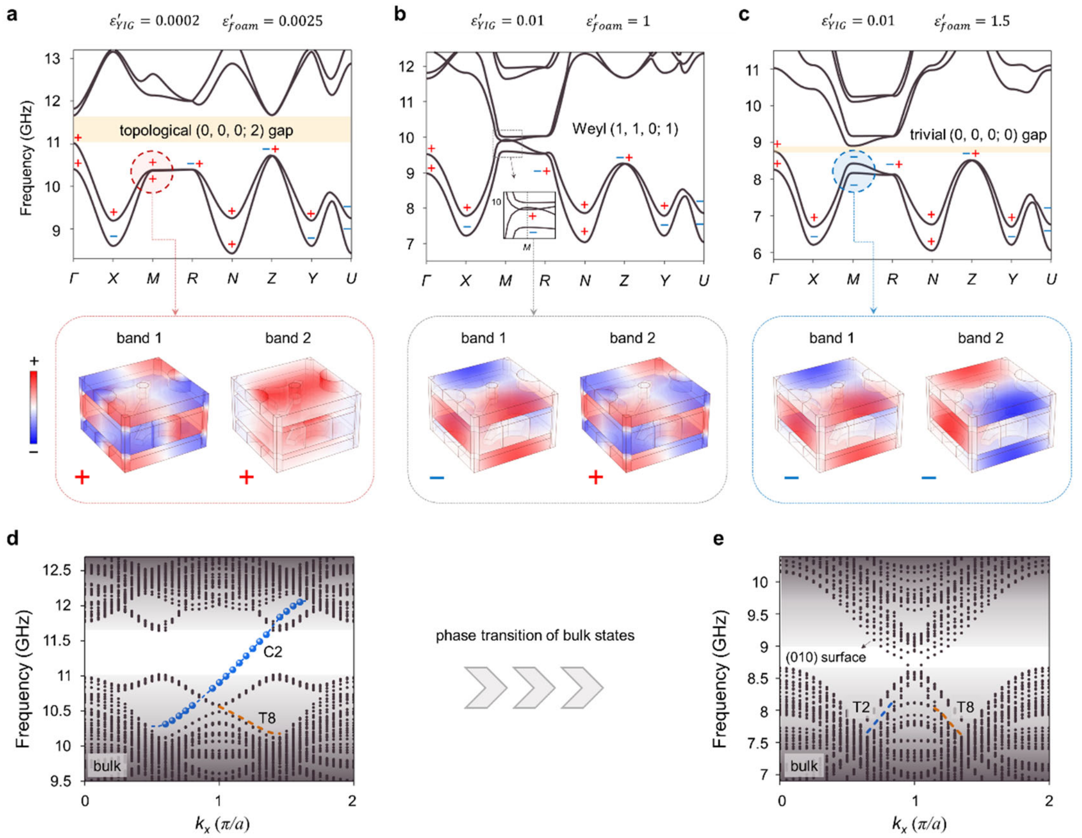

Supplementary Fig. 18 | Non-radiative loss-induced topological phase transition. a-c, Bulk band structures under continuously increasing the non-radiative loss. The lower panels show the Bloch field distributions (real part of z-component electric field) of the two lower bands at M point. Symbol +/− represent the even/odd parity. **d-e,** Projected band structures for case **a** and case **c**.

As the non-radiative loss continuously increases, the bulk bandgap will close near the M point to form a semimetal phase (Supplementary Fig. 18b), then reopen to form a trivial insulator phase (Supplementary Fig. 18c). According to the even/odd parity of Bloch field distributions at eight inversion-invariant momenta, the $\mathbb{Z}_4$ topological index changes from 2 (axion insulator phase) to 1 (Weyl semimetal phase) and then to 0 (trivial insulator phase), indicating the phase transition.